



A nitrogen-rich atmosphere on ancient Mars consistent with isotopic evolution models

Renyu Hu^{1,2}✉ and Trent B. Thomas^{1,3}

The ratio of nitrogen isotopes in the Martian atmosphere is a key constraint on the planet's atmospheric evolution. However, enrichment of the heavy isotope expected due to atmospheric loss from sputtering and photochemical processes is greater than measurements. A massive, multi-bar early CO₂-dominated atmosphere and recent volcanic outgassing have been proposed to explain this discrepancy, and many previous models have assumed atmospheric nitrogen rapidly reached a steady state where loss to space balanced volcanic outgassing. Here we show using time-dependent models that the abundance and isotopic composition of nitrogen in the Martian atmosphere can be explained by a family of evolutionary scenarios in which the initial partial pressure of nitrogen is sufficiently high that a steady state is not reached and nitrogen levels gradually decline to present-day values over 4 billion years. Our solutions do not require a multi-bar early CO₂ atmosphere and are consistent with volcanic outgassing indicated by both geologic mapping and the atmospheric ³⁶Ar/³⁸Ar ratio. Monte Carlo simulations that include these scenarios estimate that the partial pressure of N₂ was 60–740 mbar (90% confidence, with a median value of 310 mbar) at 3.8 billion years ago when the valley networks formed. We suggest that such a high nitrogen partial pressure could have contributed substantially to warming on early Mars.

We have constructed a multi-functional model for the evolution of the nitrogen abundance and isotopic composition in Mars's atmosphere and regolith, with volcanic outgassing, escape to space and nitrate deposition as sources and sinks (Methods and Extended Data Fig. 1). The model starts at 3.8 billion years ago (Ga), that is, after the last major impact (~3.9 Ga (refs. ^{1,2})), and from a $\delta^{15}\text{N}$ value of the mantle component measured in the Martian meteorite ALH 84001³. $\delta^{15}\text{N}$ is defined as the relative enhancement of the ratio $^{15}\text{N}/^{14}\text{N}$ with respect to a reference standard (Earth's atmosphere). During the modelled period, the escape processes include photochemical escape, sputtering and ion escape. We seek to reproduce the present-day size and isotopic composition of the N₂ reservoir⁴. The model has seven parameters, listed in Table 1, to capture the uncertainty in the rates of escape, volcanic outgassing and nitrate deposition, as well as the extent of diffusive fractionation between the bulk atmosphere and the exobase, where escape takes place.

Compared with previous evolutionary models of Mars nitrogen^{5–12} (Supplementary Information A), new aspects of this model include (1) a revised photochemical escape rate and fractionation factor, (2) inclusion of nitrate deposition guided by its recent discovery^{13,14}, (3) constraints of the volcanic outgassing history from argon isotopes¹⁵ and (4) coupling with the CO₂ evolutionary histories constrained by carbon isotopes¹⁶. We have made a substantial revision to the escape rate of the photodissociation of N₂ and have calculated the fractionation factor in this process, using the photochemical isotope effect method¹⁶ and the recent experimental results on the N₂ photodissociation channels¹⁷ (Supplementary Information B). Because the escape rate of nitrogen is also proportional to the mixing ratio of N₂ with respect to CO₂ when nitrogen is a relatively minor species in the atmosphere, the nitrogen evolution model must be coupled with evolutionary scenarios of CO₂. We have applied representative CO₂ evolutionary scenarios¹⁶, where

the initial pressure ranges from 0.25 to 1.8 bar (Extended Data Fig. 2), and adopted the CO₂ scenario with an initial partial pressure of 1.0 bar as the default because it may be more consistent with the comprehensive extrapolation from Mars Atmosphere and Volatile Evolution (MAVEN) measurements^{18,19} and required to cause water ice melting on early Mars's surface^{20,21}.

Bifurcation

We discovered a bifurcation between the evolutionary tracks of atmospheric N₂ starting from a low partial pressure and those from a high one. The low-start solutions feature the 'steady state', where atmospheric loss balances outgassing and nitrate deposition, while the high-start solutions never reach the steady state (Fig. 1). When the initial N₂ partial pressure is low, the rate of atmospheric escape quickly converges to the combined rate of outgassing and nitrate deposition, that is, the steady state. Over a wide range of the initial pressure, it takes a few to a few hundred million years to reach the steady state. The time it takes, however, does increase for a higher initial pressure. When the initial pressure is high enough (for example, a few hundred millibars or more), the steady state is never reached within the age of the Solar System, and a different family of evolutionary tracks emerges. We call this new family 'dynamical'. The dynamical tracks have a protracted descent of the partial pressure of N₂ during evolution rather than a speedy descent to the steady state. While the steady-state tracks converge to the same final partial pressure, the dynamical tracks lead to different final partial pressures depending on the initial value. For the same set of parameters, the final pressures of the dynamical tracks are always higher than the final pressure of the steady-state tracks (Fig. 1).

The bifurcation can be understood with the help of the following idealized and analytical model. Let X be the size of the nitrogen reservoir, V be the addition rate to this reservoir by volcanic outgassing (discounted by the rate of nitrate deposition, if any) and

¹Jet Propulsion Laboratory, California Institute of Technology, Pasadena, CA, USA. ²Division of Geological and Planetary Sciences, California Institute of Technology, Pasadena, CA, USA. ³Department of Earth and Space Sciences/Astrobiology Program, University of Washington, Seattle, WA, USA.

✉e-mail: renyu.hu@jpl.nasa.gov

Table 1 | Parameters of the nitrogen evolution model

Parameter	Symbol	Unconstrained MCMC	Constrained MCMC
Power-law index of photochemical loss	a	0.5–3.0	0.5–3.0
Multiplier of photochemical loss	f_{pr}	0.001–100,000	0.001–2,000
Multiplier of sputtering loss	f_{sp}	0.001–100,000	0.001–2,000
Multiplier of volcanic outgassing	f_{og}	0.001–100,000	0.001–2,000
Diffusion parameter (km K^{-1})	$\Delta z/T$	0.2–0.5	0.2–0.5
Depth of nitrate deposition (m)	d	0.001–1,000,000	0.001–1,000,000
Partial pressure of N_2 at 3.8 Ga (mbar)	$P_{3.8\text{Ga}}$	0.001–1,000,000	0.001–1,000,000

The photochemical escape rate is extrapolated from the current-epoch estimate using a power-law scaling to the solar EUV flux. Multipliers are then applied to the baseline models of photochemical loss, sputtering loss and volcanic outgassing to allow exploration of the strengths of these processes. The constrained MCMCs apply plausible upper limits of the multipliers, and the unconstrained MCMCs explore the multipliers in essentially unlimited ranges. The diffusion parameter is the difference between the altitude of the homopause and the exobase divided by the temperature in this interval, and this parameter has been measured by MAVEN²³. Finally, the depth of nitrate deposition describes how much nitrate has formed and been sequestered in the crust. Full definitions of these parameters are provided in Methods.

E be the escape rate. When the size of the nitrogen reservoir is small compared with the carbon reservoir, the escape is proportional to its size (Methods), and at the limit of a constant background CO_2 pressure, we can write $E = eX$, where e is a coefficient. The equation for X is then

$$\frac{dX}{dt} = V - eX. \quad (1)$$

For a constant V and e , the equation has the following solution

$$X = \frac{V}{e} + \left(X_0 - \frac{V}{e} \right) \exp(-et), \quad (2)$$

where X_0 is X at $t=0$. Therefore, the solution converges to the steady state with a timescale of $1/e$. Note that the solution in equation (2), despite its idealized nature, is quite similar to the segment of a given steady-state solution that rapidly approaches the steady state (Fig. 1). Currently, the $1/e$ timescale for sputtering loss is $\sim 4,000$ Myr (ref. ²²), and that for photochemical loss is $\sim 1,000$ Myr (ref. ⁸). The corresponding timescales were ~ 2 Myr and ~ 70 Myr (for a power-law index of 1.5) at 3.5 Ga when the solar extreme ultraviolet (EUV) flux was approximately six times the current value (Methods). These estimates tell us that (1) it is possible to reach the steady state early in the evolution and becomes harder as time goes by, and (2) sputtering loss is the main process that drives the system to the steady state in the early epoch (because of its small $1/e$ timescale).

Then why do some evolutionary tracks never reach the steady state? This is because the sputtering rate is no longer proportional to the size of the nitrogen reservoir when the atmosphere is moderately nitrogen rich (see equation (9) in Methods). The sputtering rate decouples when the size of the nitrogen reservoir approaches the size of the carbon reservoir, corrected by the diffusive separation factor between N_2 and CO_2 . This factor is ~ 8 for typical upper-atmosphere conditions²³, implying that N_2 cannot be considered a minor component for determining the sputtering rate when

it is approximately 10% or more in the bulk atmosphere. Because of this decoupling, E can no longer be written as eX and the steady state no longer exists. The bifurcation can thus be understood as such: when the initial nitrogen pressure is small, the system can quickly reach the steady state following the solution in equation (2); when the initial nitrogen pressure is large, the atmosphere must first lose nitrogen relative to carbon, on a linear rather than exponential time dependency, and by the time it starts to converge to the steady state, the $1/e$ timescale is already large, and then the steady state can never be reached within the age of the Solar System.

Steady-state and dynamical solutions

The present-day size and isotopic composition of the nitrogen reservoir can be matched by either the steady-state or the dynamical evolution tracks by adjusting the parameters for the rates of outgassing and escape. Figure 2 shows example steady-state and dynamical solutions. In these solutions, sputtering removes most of the mass in total, while photochemical escape takes over as the dominant mass-loss mechanism around 1–2 Ga. In the dynamical solution, the initial partial pressure is 238 mbar, and sputtering removes 212 mbar and photochemical escape removes 23 mbar. Nitrate deposition, which can be comparable to volcanic outgassing rates >3 Ga, is not a dominant sink in the more recent history. Outgassing is an important process in the recent history, and as a result, specific implementation of the baseline outgassing model (Extended Data Fig. 3) can affect the evolutionary outcome.

For the steady-state solutions shown in Fig. 2, increasing the initial partial pressure to a critical value of ~ 1.2 bar does not change the evolutionary outcome, but an even higher initial pressure would lead to bifurcation and a dynamical track. That track is no longer a solution because the final pressure would be too high. For the dynamical solution shown in Fig. 2, which uses smaller rate multipliers (f_{sp} and f_{pr}) compared with the steady-state solutions, an initial partial pressure of ~ 240 mbar already causes the dynamical evolution. Further decreasing the initial partial pressure would result in a steady-state track in this case, but that track is not a solution either because the final $\delta^{15}\text{N}$ would be substantially smaller than the observed. From these examples, we make the following three observations. (1) The insensitivity to the initial pressure of the steady-state solutions is consistent with the understanding in the past that the memory of the initial state is ‘lost’ for the nitrogen evolution¹². However, this understanding applies only to the scenarios where the initial partial pressure is less than a critical value at which the bifurcation occurs. (2) The critical pressure increases for higher escape rates or greater photochemical loss and sputtering multipliers (f_{pr} and f_{sp}). (3) The dynamical solutions are typically the evolution tracks that are quite close to the transitional track between the steady-state and the dynamical tracks. This is not surprising because the final partial pressures of the dynamical tracks quickly diverge to large values, which would be inconsistent with present-day Mars (Fig. 1). As a result of this adjacency to the steady-state solutions, the final isotopic composition only moderately depends on the initial value (Fig. 2). Because of all these features, if the dynamical solutions indeed apply to Mars, the current isotopic composition can be used to infer the partial pressure of nitrogen in the past.

A nitrogen-rich early Martian atmosphere

We have systematically explored the potential evolutionary paths of Mars nitrogen with the Markov-Chain Monte Carlo (MCMC) method to fit the present-day partial pressure and isotopic composition. Using the parameters listed in Table 1, we have run ‘unconstrained MCMC’, where the rate multipliers are allowed to vary in wide ranges, and ‘constrained MCMC’, where the outgassing multiplier is allowed to vary only within the upper limit derived from argon isotopes¹⁵ and the escape rates are allowed to vary up to twice the baseline models^{8,22}. Because the baseline volcanism

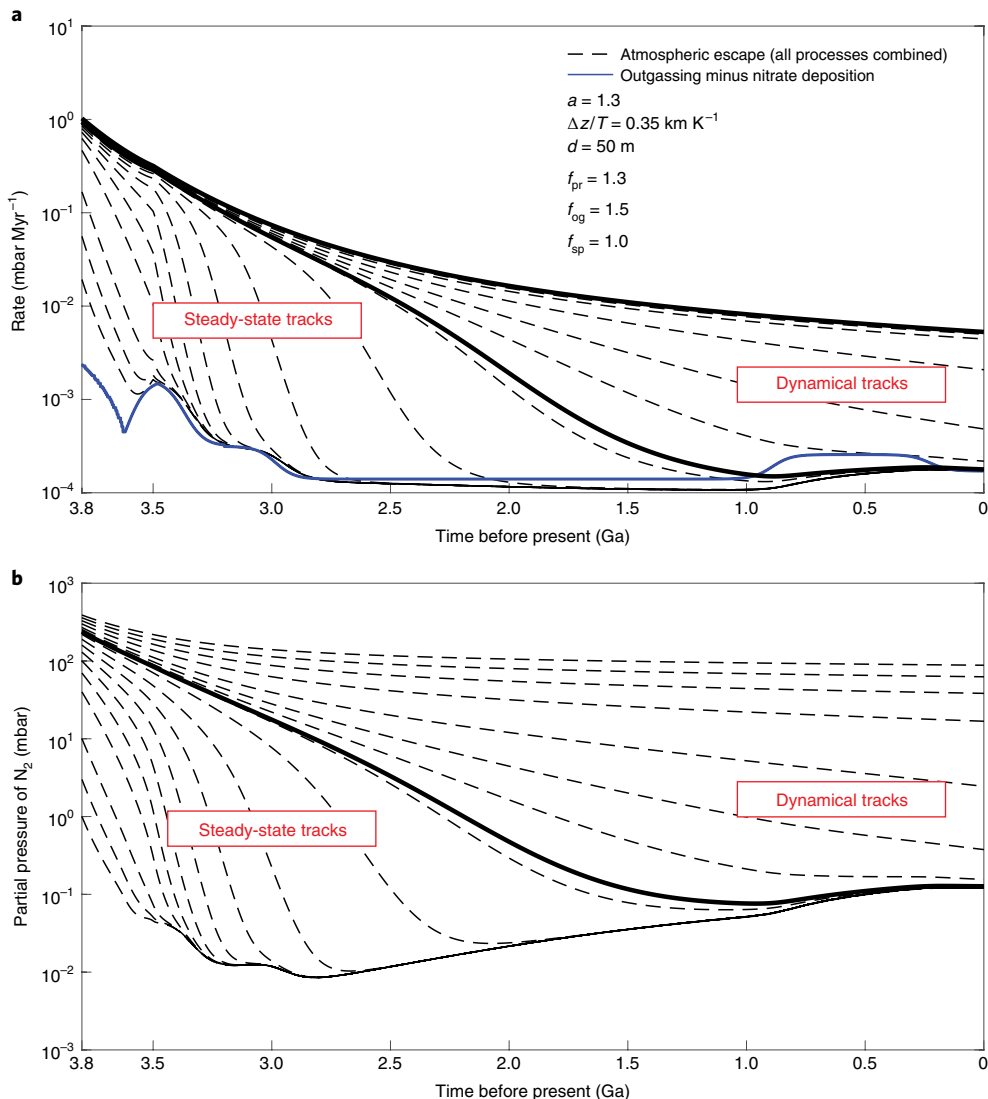


Fig. 1 | Bifurcation in the evolution of nitrogen between the steady-state scenarios and the dynamical scenarios. **a,b**, Change rates (**a**) and the partial pressure (**b**) of N_2 for evolutionary tracks with the same set of parameters but different initial pressures. When the initial pressure is greater than a critical value, the steady state cannot be reached by the end, and a new set of dynamical scenarios emerges. The transitional track from this critical initial pressure is shown in a thick line, and it separates the steady-state and the dynamical scenarios.

model is consistent with the one adopted in the argon isotope study (Extended Data Fig. 3), the argon-based constraint is applicable here to the extent that Mars's mantle has a similar N/Ar ratio to Earth. The constrained MCMCs can thus be understood as exploring the scenarios permitted by the argon isotopes and the current understanding of nonthermal escape from Mars. The posterior distributions of parameters are shown in Extended Data Figs. 4–6, and solutions randomly selected from the unconstrained and constrained MCMCs are shown in Fig. 3.

When there is essentially no limit on the rate multipliers, the steady-state solutions can be found with large escape and outgassing rates (Supplementary Information E). When we impose the upper limits on the rate multipliers (the constrained MCMCs), the escape rates are smaller, and thus the solutions take a longer time to reach the corresponding steady states, or cannot reach the steady states at all (Fig. 3). In this case, the initial partial pressure of N_2 is constrained despite all other model parameters (Extended Data Figs. 5 and 6) and is not sensitive to the specific implementation of the baseline outgassing model, the initial $\delta^{15}\text{N}$ value or potential

variation of the $\Delta z/T$ parameter over the course of evolution (Supplementary Information F). The spread in the posterior distribution of the initial pressure comes mainly from the uncertainty of the sputtering rate as sputtering is the dominant mass removal mechanism. Extended Data Fig. 6 shows that the posterior distribution becomes very narrow when the sputtering multiplier is fixed and moves to higher values when the multiplier increases.

For the sputtering rate within a factor of two from the current estimate²², the evolution model constrains the partial pressure of nitrogen at 3.8 Ga to 60–740 mbar (90% confidence), with a median value of 310 mbar (Extended Data Fig. 5). The median value increases to 370 mbar when the atmosphere collapse is enforced. While we caution against placing too much emphasis on these specific values, the MCMCs clearly indicate that many solutions favour a nitrogen-rich early Martian atmosphere. The ability to constrain the early abundance of N_2 fundamentally comes from the solutions being (close to) dynamical when the realistic constraints from argon isotopes and nonthermal escape models are imposed. We thus suggest that the dynamical solutions or the solutions that reach the

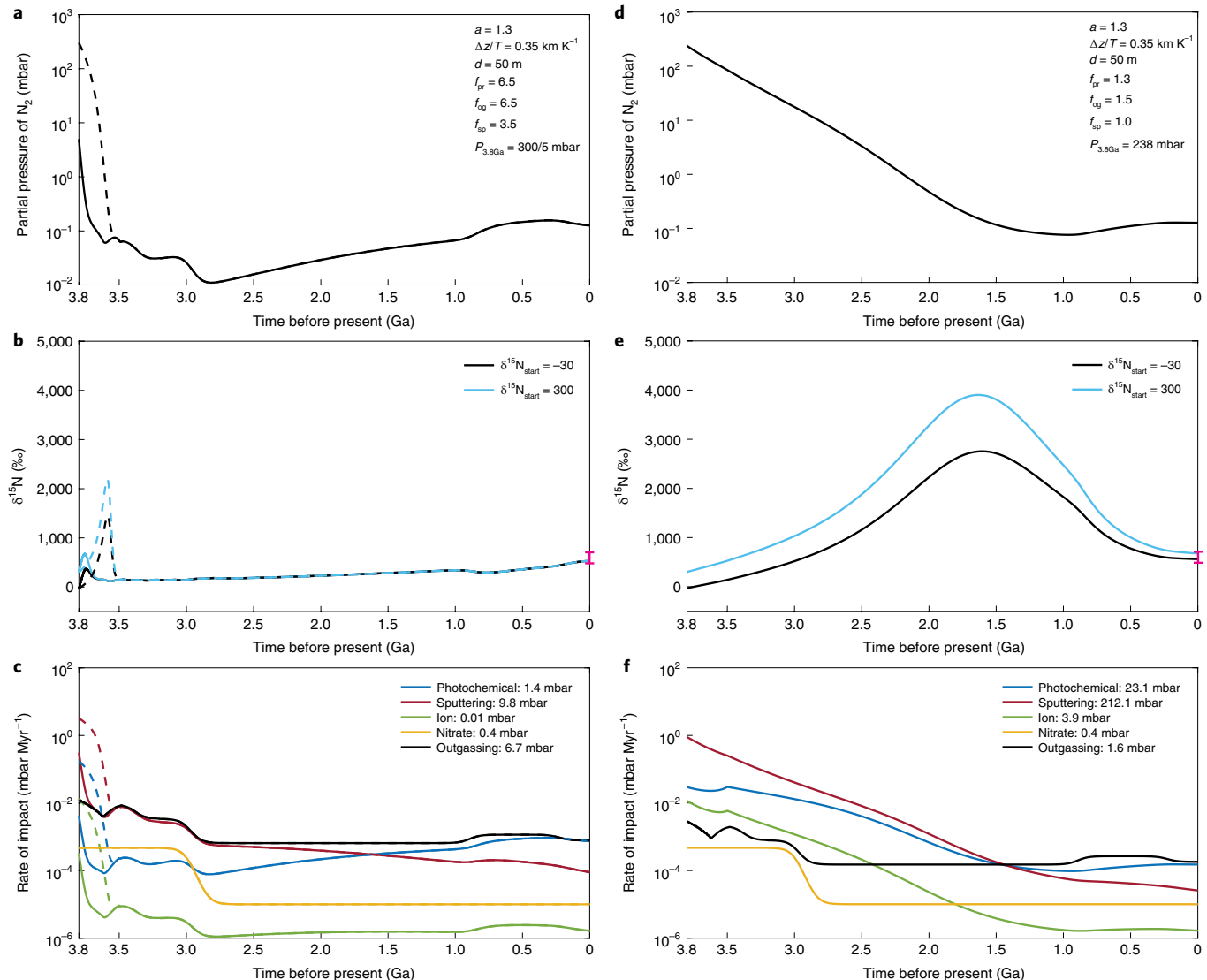


Fig. 2 | Example of the steady-state and dynamical solutions consistent with the size and isotopic composition of Mars's nitrogen reservoir. a–f,

These models adopt the CO_2 evolutionary scenario 3 with the initial partial pressure of 1.0 bar (Extended Data Fig. 2). Two steady-state solutions with different initial pressures are shown with solid and dashed lines (a–c). In b and e, the solutions starting with an elevated initial $\delta^{15}\text{N}$ of 300‰ (ref. ¹²) are shown in blue for comparison, and the error bar in purple is the Curiosity measurement⁴. In c and f, the labels show the total mass added or removed by each process for the solutions shown in the solid lines. The steady-state (a–c) and dynamical (d–f) solutions require distinct parameters to match the present-day abundance and isotopic composition.

steady states late in the evolution may better represent the evolutionary history of nitrogen on Mars.

The dynamical solutions imply an N_2 -rich atmosphere on early Mars, for which the escape rate of carbon would be reduced compared with the rate for a CO_2 -dominated atmosphere. We thus present models of the CO_2 – N_2 evolution that include this feedback in Supplementary Information G. In essence, self-consistent solutions can be found with small changes of the input parameters, and the character of the steady-state and dynamical solutions remains unchanged. While the high initial N_2 in the dynamical solutions may suppress the escape of carbon, the amount of early carbonate deposition is poorly constrained¹⁶, and so is the initial partial pressure of CO_2 . Extended Data Figs. 4 and 5 show that the nitrogen evolution models and the associated constraints on nitrogen's partial pressure at 3.8 Ga are insensitive to the specifics of the adopted CO_2 evolutionary history in the wide range that has been explored.

Therefore, an initially large N_2 reservoir preferred by the isotopic constraints is fully compatible with an initially large CO_2 reservoir.

One might ask, if Mars started with nearly equal abundances of N_2 and CO_2 in the atmosphere, why does it currently have a CO_2 -dominated atmosphere? The atmospheric composition is deflected towards CO_2 dominance because N_2 is much more prone than CO_2 to sputtering loss. With equal mixing ratios in the bulk atmosphere, the sputtering loss rate of N_2 is ~32 times higher than that of CO_2 , with a factor of ~8 from diffusive enrichment and a factor of ~4 from the difference in the sputtering yield (see equation (7) in Methods). Thus, sputtering can gradually reduce the abundance of N_2 with respect to CO_2 , followed by the approach to the steady state, to establish the CO_2 -dominated atmosphere. This preferential loss of N_2 versus CO_2 may well be a common feature of nonthermal escape from unmagnetized planets and might affect the evolutionary outcomes of terrestrial exoplanets.

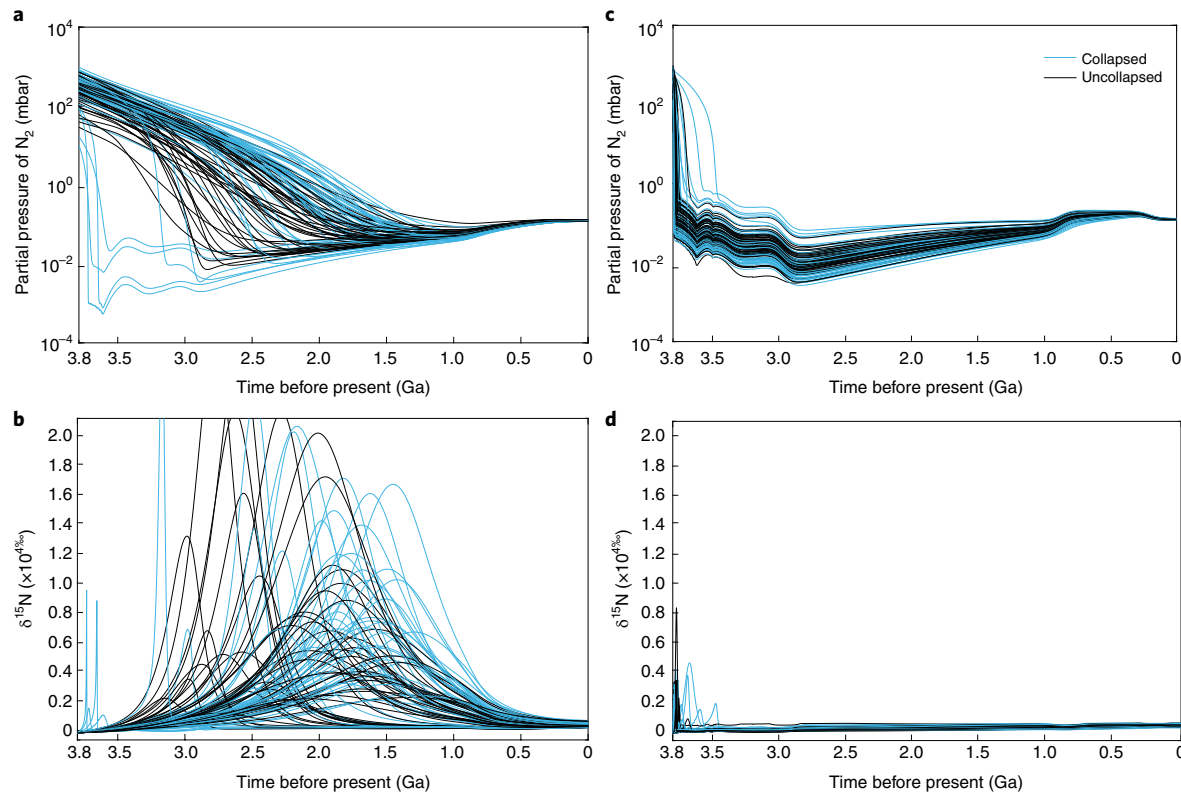


Fig. 3 | Randomly selected solutions from the constrained and the unconstrained MCMCs. **a-d**, These models use the CO₂ evolutionary scenario 3 with the initial partial pressure of 1.0 bar or the collapsed atmosphere scenario (scenario 5 in Extended Data Fig. 2). Each line represents an evolution path that meets the present-day partial pressure (**a,c**) and isotopic composition of N₂ (**b,d**). Most solutions from the unconstrained MCMCs (**c,d**) are solutions that quickly converge to the steady states, and most solutions from the constrained MCMCs (**a,b**) are dynamical solutions, or solutions that reach the steady states late in the evolution.

Another question is how to form the nitrogen-rich atmosphere on Mars in the first place. The ratio between CO₂ and N₂ was probably >10 in volcanic outgassing^{24–26}. Thus, we speculate that the atmosphere at 3.8 Ga came primarily from late veneer of primitive bodies such as comets that have low C/N ratios²⁷ after the atmosphere built by earlier volcanic outgassing had been removed by hydrodynamic escape²⁸. If the cometary origin was the case, the initial $\delta^{15}\text{N}$ might be higher than what we have assumed (~800‰ (ref. ²⁹)). Nonetheless, the evolution models and isotope-based constraints are not sensitive to this variation of the initial $\delta^{15}\text{N}$.

Measurements of future in situ or sample return exploration can further delineate the steady-state versus dynamical nitrogen evolution. Figure 3 shows that the $\delta^{15}\text{N}$ value of the dynamical solutions has a broad peak between 3.5 and 1 Ga (the Hesperian and early Amazonian periods), and that of the steady-state solutions does not. The magnitude of the peaks with a non-collapsed atmosphere is ~5,000–20,000‰, and that with a collapsed atmosphere can be even larger. If some of this signal is transferred to the nitrates formed, isotopic analyses of nitrate samples could provide additional evidence for the dynamical evolution of nitrogen as well as the atmospheric collapse in the history of Mars.

Under the new interpretation of nitrogen's isotopic composition presented here, a few hundred millibars N₂ may have existed in the Martian atmosphere at 3.8 Ga. Previous one-dimensional (1D) radiative-convective climate models have determined that this amount of additional nitrogen could cause the mean surface temperature to be ~10 K warmer than a pure, 1 bar CO₂ atmosphere via pressure broadening of CO₂ absorption bands²¹. The additional few hundred millibars N₂, coupled with substantial early carbonate deposition, may thus be particularly meaningful for sustaining

surface melting at low topographic regions²⁰. The climate conditions on early Mars have been a conundrum^{30–32}, and our findings may provide a new path forward for explaining the geologic records³³ that suggest persisting liquid-water conditions on ancient Mars's surface.

Online content

Any methods, additional references, Nature Research reporting summaries, source data, extended data, supplementary information, acknowledgements, peer review information; details of author contributions and competing interests; and statements of data and code availability are available at <https://doi.org/10.1038/s41561-021-00886-y>.

Received: 27 May 2020; Accepted: 16 December 2021;
Published online: 10 February 2022

References

1. Fassett, C. I. & Head, J. W. Sequence and timing of conditions on early Mars. *Icarus* **211**, 1204–1214 (2011).
2. Robbins, S. J., Hynek, B. M., Lillis, R. J. & Bottke, W. F. Large impact crater histories of Mars: the effect of different model crater age techniques. *Icarus* **225**, 173–184 (2013).
3. Mathew, K. & Marti, K. Early evolution of Martian volatiles: nitrogen and noble gas components in ALH84001 and Chassigny. *J. Geophys. Res. Planets* **106**, 1401–1422 (2001).
4. Wong, M. H. et al. Isotopes of nitrogen on Mars: atmospheric measurements by Curiosity's mass spectrometer. *Geophys. Res. Lett.* **40**, 6033–6037 (2013).
5. McElroy, M. B. & Yung, Y. L. Isotopic composition of the Martian atmosphere. *Science* **194**, 68–70 (1976).
6. McElroy, M. B., Yung, Y. L. & Nier, A. O. Isotopic composition of nitrogen: implications for the past history of Mars' atmosphere. *Science* **194**, 70–72 (1976).

7. Fox, J. L. & Dalgarno, A. Nitrogen escape from Mars. *J. Geophys. Res. Space Phys.* **88**, 9027–9032 (1983).
8. Fox, J. L. The production and escape of nitrogen atoms on Mars. *J. Geophys. Res. Planets* **98**, 3297–3310 (1993).
9. Jakosky, B. M., Pepin, R. O., Johnson, R. E. & Fox, J. L. Mars atmospheric loss and isotopic fractionation by solar-wind-induced sputtering and photochemical escape. *Icarus* **111**, 271–288 (1994).
10. Zent, A. P. & McKay, C. P. The chemical reactivity of the Martian soil and implications for future missions. *Icarus* **108**, 146–157 (1994).
11. Fox, J. L. & Hać, A. The $^{15}\text{N}/^{14}\text{N}$ isotope fractionation in dissociative recombination of N_2^+ . *J. Geophys. Res. Planets* **102**, 9191–9204 (1997).
12. Kurokawa, H., Kurosawa, K. & Usui, T. A lower limit of atmospheric pressure on early Mars inferred from nitrogen and argon isotopic compositions. *Icarus* **299**, 443–459 (2018).
13. Stern, J. C. et al. Evidence for indigenous nitrogen in sedimentary and Aeolian deposits from the Curiosity rover investigations at Gale Crater. *Mars. Proc. Natl Acad. Sci. USA* **112**, 4245–4250 (2015).
14. Sutter, B. et al. Evolved gas analyses of sedimentary rocks and eolian sediment in Gale Crater, Mars: results of the Curiosity rover's sample analysis at Mars instrument from Yellowknife Bay to the Namib Dune. *J. Geophys. Res. Planets* **122**, 2574–2609 (2017).
15. Slipksi, M. & Jakosky, B. M. Argon isotopes as tracers for Martian atmospheric loss. *Icarus* **272**, 212–227 (2016).
16. Hu, R., Kass, D. M., Ehmann, B. L. & Yung, Y. L. Tracing the fate of carbon and the atmospheric evolution of Mars. *Nat. Commun.* **6**, 10003 (2015).
17. Song, Y. et al. Quantum-state dependence of product branching ratios in vacuum ultraviolet photodissociation of N_2 . *Astrophys. J.* **819**, 23 (2016).
18. Jakosky, B. M. et al. Loss of the Martian atmosphere to space: present-day loss rates determined from MAVEN observations and integrated loss through time. *Icarus* **315**, 146–157 (2018).
19. Jakosky, B. M. The CO_2 inventory on Mars. *Planet. Space Sci.* **175**, 52–59 (2019).
20. Forget, F. et al. 3d modelling of the early Martian climate under a denser CO_2 atmosphere: temperatures and CO_2 ice clouds. *Icarus* **222**, 81–99 (2013).
21. von Paris, P., Grenfell, J. L., Rauer, H. & Stock, J. W. N_2 -associated surface warming on early Mars. *Planet. Space Sci.* **82**, 149–154 (2013).
22. Leblanc, F. & Johnson, R. Role of molecular species in pickup ion sputtering of the Martian atmosphere. *J. Geophys. Res. Planets* <https://doi.org/10.1029/2000JE001473> (2002).
23. Jakosky, B. M. et al. Mars' atmospheric history derived from upper-atmosphere measurements of $^{38}\text{Ar}/^{36}\text{Ar}$. *Science* **355**, 1408–1410 (2017).
24. McKay, C. P. & Stoker, C. R. The early environment and its evolution on Mars: implication for life. *Rev. Geophysics* **27**, 189–214 (1989).
25. Marty, B. & Dauphas, N. The nitrogen record of crust–mantle interaction and mantle convection from Archean to present. *Earth Planet. Sci. Lett.* **206**, 397–410 (2003).
26. Hirschmann, M. M. & Withers, A. C. Ventilation of CO_2 from a reduced mantle and consequences for the early Martian greenhouse. *Earth Planet. Sci. Lett.* **270**, 147–155 (2008).
27. Bergin, E. A., Blake, G. A., Ciesla, F., Hirschmann, M. M. & Li, J. Tracing the ingredients for a habitable Earth from interstellar space through planet formation. *Proc. Natl Acad. Sci. USA* **112**, 8965–8970 (2015).
28. Tian, F., Kasting, J. F. & Solomon, S. C. Thermal escape of carbon from the early Martian atmosphere. *Geophys. Res. Lett.* **36**, L02205 (2009).
29. Marty, B. The origins and concentrations of water, carbon, nitrogen and noble gases on Earth. *Earth Planet. Sci. Lett.* **313**, 56–66 (2012).
30. Ramirez, R. M. et al. Warming early Mars with CO_2 and H_2 . *Nat. Geosci.* **7**, 59–63 (2014).
31. Kite, E. S. et al. Methane bursts as a trigger for intermittent lake-forming climates on post-Noachian Mars. *Nat. Geosci.* **10**, 737–740 (2017).
32. Wordsworth, R. et al. Transient reducing greenhouse warming on early Mars. *Geophys. Res. Lett.* **44**, 665–671 (2017).
33. Grotzinger, J. et al. Deposition, exhumation, and paleoclimate of an ancient lake deposit, Gale Crater, Mars. *Science* **350**, aac7575 (2015).

Publisher's note Springer Nature remains neutral with regard to jurisdictional claims in published maps and institutional affiliations.

© The Author(s), under exclusive licence to Springer Nature Limited 2022

Methods

Overview. The model starts at 3.8 Ga and simulates the loss and addition of N₂ in a combined reservoir of the atmosphere and the regolith (by adsorption) until the present day. It includes five addition and loss mechanisms shown in Extended Data Fig. 1. When tracing the evolution, the model uses a variable time step adapted to allow no more than 0.05% change in the N₂ reservoir per step. This ensures that the temporal resolution is high enough to capture important details of the atmosphere's evolution.

An evolutionary solution must reach the present-day size and isotopic composition of the N₂ reservoir. The size of the atmospheric reservoir is 0.12 mbar, and that of the regolith reservoir is up to 0.01 mbar (ref. ³⁴). The upper limit corresponds to adsorption in up to 10 m global equivalent of the Martian regolith having ~20 m² g⁻¹ surface area (ref. ³⁵). The isotopic composition of the present-day nitrogen reservoir is δ¹⁵N = 572 ± 82‰ (ref. ⁴). We do not include potential fractionation between the atmosphere and the regolith because the regolith reservoir size is minor compared with the atmosphere.

The initial size of the nitrogen reservoir is a free parameter of the model. The initial δ¹⁵N value of the reservoir, however, is uncertain. For the nominal cases, we assume the initial reservoir to have the isotopic composition of the mantle component of the nitrogen measured in the Martian meteorite ALH 84001³ (δ¹⁵N = -30‰). Nonetheless, escape and giant impacts that occurred before the modelled period may have modified the δ¹⁵N value from the mantle value, and previous estimates suggest that the δ¹⁵N value can vary rapidly between the mantle value and up to 500‰ more than 3.8 Ga (ref. ¹²). We thus explore the effect of an elevated initial δ¹⁵N value (for example, 300‰, Supplementary Information F).

To calculate the mixing ratio of N₂ (needed for calculating the escape rates), the model is coupled with an evolution model of CO₂ (ref. ¹⁶) for the same modelled period. The model of CO₂ includes photochemical loss, sputtering loss, volcanic outgassing and carbonate deposition¹⁶, but not the feedback of the N₂ mixing ratio on the escape rates of carbon. We present fully coupled carbon and nitrogen evolution models in Supplementary Information G. Otherwise, we explore nitrogen's evolutionary history by adopting the CO₂ evolutionary scenarios with an initial partial pressure of CO₂ ranging from 0.25 to 1.8 bar (Scenarios 1–4 in Extended Data Fig. 2). These scenarios are selected to represent a wide range of possible CO₂ evolutionary tracks. In essence, carbon's isotopic composition constrains the relative strengths between photochemical loss and carbonate deposition, while the amount of carbonate deposition—and thus the initial pressure—can typically vary by a few hundred millibars due to the range in the possible timing and fractionation factor of carbonate deposition, as well as the uncertainties in the carbon isotope's measurement, outgassing models and sputtering rates. The representative scenarios adopted here approximately encompass the lower and upper bounds of the CO₂ partial pressure at 3.8 Ga allowed by the carbon isotopic composition¹⁶.

We also include the endmember scenario of a collapsed atmosphere (Scenario 5 in Extended Data Fig. 2). It has been suggested that the atmosphere of Mars can collapse to form large polar CO₂ ice caps during low-obliquity periods, and the remaining atmosphere would be in vapour pressure balance with the ice caps^{20,36,37}. The collapse of CO₂ may matter for the evolution of nitrogen because it greatly increases the mixing ratio of N₂ in the atmosphere. For example, the latest nitrogen evolution model¹² assumed that atmospheres with CO₂ partial pressure <500 mbar collapse. Here we explore the effect of the collapse with an endmember scenario where the atmosphere is considered always 'collapsed', that is, maintaining a CO₂ partial pressure of 7 mbar.

Photochemical escape. The photochemical escape rate of nitrogen (F_{pr}) is modelled as

$$F_{\text{pr}} = F_{0,\text{pr}} \left(\frac{F_{\text{EUV}}}{F_{0,\text{EUV}}} \right)^a \frac{X_{\text{N}_2}}{X_{0,\text{N}_2}} f_{\text{pr}}, \quad (3)$$

where the quantities with the subscript ₀ are at the current epoch, F_{EUV} is the solar EUV flux for which we adopt as $F_{\text{EUV}} \approx t^{-1.23}$ where t is the age^{38–40}, X_{N_2} is the mixing ratio of N₂ in the bulk atmosphere, a is a power-law index and f_{pr} is a multiplication factor. The photochemical escape rate is proportional to the mixing ratio of N₂ in the atmosphere⁷. The power-law index and the multiplication factor provide sufficient freedom for the model to capture the uncertainties in the photochemical escape rate and how it has changed with the solar input. This parameterization also consolidates the uncertainty in the age dependency of the solar EUV flux into a (Supplementary Information F).

We break down the photochemical escape into major escape mechanisms because they have different isotopic fractionation factors, as

$$F_{\text{pr}} = F_{\text{photo}} + F_{\text{recom}} + F_{\text{chem}}, \quad (4)$$

where F_{photo} , F_{recom} and F_{chem} are the rates of escape produced by photodissociation and photoionization, dissociative recombination and other chemical reactions, respectively. The current-epoch rates of these processes are baselined by the upper-atmosphere models of ref. ⁸, except for the photodissociation escape rate, which we reevaluated in Supplementary Information B. We assume that the

scaling in equation (3) applies equally to these processes. Technically speaking, the photodissociation escape is driven by higher-energy parts of the solar EUV flux (for example, the Lyman continuum) and should have a different scaling. Applying the same scaling, however, is not a problem because we find that the photodissociation escape rate turns out to be minimal.

The isotopic fractionation factor (α) of each of these processes is the product of the fractionation factor due to diffusive separation from the homopause to the exobase (α_{diffu}) and the fractionation factor when the escaping particles are launched by these processes near the exobase ($\alpha_{\text{photo/recom/chem}}$), as

$$\alpha = \alpha_{\text{diffu}} \alpha_{\text{photo/recom/chem}}. \quad (5)$$

The diffusive separation is modelled as

$$\alpha_{\text{diffu}} = \exp \left(\frac{-g\Delta m \Delta z}{kT} \right), \quad (6)$$

where g is Mars's surface gravity, Δm is the mass difference of the atoms or isotopologues in question, Δz is the distance from the homopause to the exobase, k is the Boltzmann constant and T is the mean temperature of the thermosphere. We include the effect of diffusive separation from the homopause all the way to the exobase, even though the peak of the photodissociation rate occurs well below the exobase⁴¹, because only the energetic particles sourced at altitudes close to the exobase have a high probability to escape^{12,43}. It is evident from equation (6) that α_{diffu} is controlled by the quantity $\Delta z/T$, which is constrained by MAVEN measurements of the argon isotopes (Supplementary Information D).

We determine α_{photo} in Supplementary Information B, adopt previous calculations¹¹ for α_{recom} (= 0.58) and assume $\alpha_{\text{chem}} = 1$. The main chemical reaction that produces escaping nitrogen is N₂⁺ + O → NO⁺ + N. This reaction produces 10.9 eV as the excess energy, and this energy is partitioned into the products as the kinetic energy⁷. The kinetic energy partitioned to N is much higher than the escape threshold energy (~1.73 eV). This process, therefore, does not strongly fractionate nitrogen. Similarly, because dissociative ionization and electron impact dissociation produce energies more than 10 eV, these processes do not strongly fractionate nitrogen in the escape.

Sputtering. Sputtering by oxygen ions picked up and propelled by the magnetic field of the solar wind can also cause escape. The loss due to sputtering is expected to be stronger at earlier epochs, when the solar EUV flux was higher. This process occurs as Mars does not have a strong magnetic field during the modelled period⁴⁴, and the atmosphere is exposed to the solar wind. To model the sputtering loss rate of N₂ (F_{sp}), we scale the sputtering rate of CO₂ ($F_{\text{sp}}(\text{CO}_2)$) by the yields and mixing ratios^{9,12,15} of N₂ and CO₂ as

$$F_{\text{sp}} = F_{\text{sp}}(\text{CO}_2) \frac{Y_{\text{N}_2}}{Y_{\text{CO}_2}} \frac{X_{\text{N}_2}}{X_{\text{CO}_2}} \alpha_{\text{diffu,N}_2/\text{CO}_2} \frac{1}{\alpha_{\text{dil}}} f_{\text{sp}}, \quad (7)$$

where Y is the yield, $\alpha_{\text{diffu,N}_2/\text{CO}_2}$ is the diffusion separation between N₂ and CO₂ calculated by equation (6) with Δm equal to the mass difference between N₂ and CO₂, f_{sp} is a multiplication factor to account for uncertainties in the flux and α_{dil} is a dilution factor that accounts for the dilution by all species at the exobase and is defined as

$$\alpha_{\text{dil}} \equiv 1 + \sum_i \frac{X_i}{X_{\text{CO}_2}} \alpha_{\text{diffu},i/\text{CO}_2}, \quad (8)$$

where $\alpha_{\text{diffu},i/\text{CO}_2}$ is the diffusion separation between the species i and CO₂ defined similarly to equation (6). In addition to N₂, we include in this sum the minor species in Mars's atmosphere, Ar, O and CO, which currently have the abundances of 1.6%, 0.13% and 0.08% by volume, respectively.

Let us consider the dependency of the sputtering rate on the size of the nitrogen reservoir. Expanding α_{dil} in equation (7), and including only the terms relevant to X_{N_2} , we have

$$F_{\text{sp}} \approx F_{\text{sp}}(\text{CO}_2) \frac{Y_{\text{N}_2}}{Y_{\text{CO}_2}} f_{\text{sp}} \frac{\frac{X_{\text{N}_2}}{X_{\text{CO}_2}} \alpha_{\text{diffu,N}_2/\text{CO}_2}}{1 + \frac{X_{\text{N}_2}}{X_{\text{CO}_2}} \alpha_{\text{diffu,N}_2/\text{CO}_2}}. \quad (9)$$

Therefore, when $\frac{X_{\text{N}_2}}{X_{\text{CO}_2}} \alpha_{\text{diffu,N}_2/\text{CO}_2} \ll 1$, the scaled sputtering rate is proportional to the size of the nitrogen reservoir, and when $\frac{X_{\text{N}_2}}{X_{\text{CO}_2}} \alpha_{\text{diffu,N}_2/\text{CO}_2} \gg 1$, the sputtering rate no longer depends on the size of the nitrogen reservoir. Because $\alpha_{\text{diffu,N}_2/\text{CO}_2} \approx 8.5$ for a typical $\Delta z/T$ of 0.3 km K⁻¹, the sputtering rate becomes decoupled from the size of the nitrogen reservoir when it approaches the size of the carbon reservoir. This decoupling gives rise to slow approach to the steady states and eventually the dynamical solutions.

We adopt the 3D Monte Carlo simulations³² as the baseline values of the sputtering rate of CO₂, fitted to the following functional form

$$F_{\text{sp}}(\text{CO}_2) = \exp(-0.462 \ln(F_{\text{EUV}}/F_{0,\text{EUV}})^2 + 5.086 \ln(F_{\text{EUV}}/F_{0,\text{EUV}}) + 53.49) \quad (10)$$

where F_{sp} in this formula is the sputtering escape flux in particles per second. The basis for this formula comes from the product of the previously calculated fluxes of the incident pickup ions⁴⁵ and the yield of escaping carbon particles²². The pickup ion fluxes calculated by ref.⁴⁵ for the current epoch are remarkably consistent with more sophisticated 3D models within a factor of two (refs.^{46,47}) and with the globally averaged precipitating ion flux and its energy spectrum measured by MAVEN⁴⁸. For the sputtering yield of N₂, we adopt the value calculated by the Monte Carlo simulations in ref.⁹ as it is the latest value.

Last, the sputtering loss is energetic enough that it does not preferentially select the escape of the N isotopes. The fractionation factor in the sputtering loss is the diffusive fractionation from the homopause to the exobase, that is, α_{diff} given by equation (6). While the pickup ion's energy is deposited principally at altitudes well below the exobase, the recoil particles are quickly thermalized if they are produced at that altitude⁴⁹. Only the particles produced near the exobase can escape. We thus use the exobase as the proxy for the source altitude of the sputtering loss.

Ion loss. Ion loss is the only nonthermal escape process that has been directly measured at Mars^{50–52}, and the measured rates of carbon (as CO₂⁺) and oxygen (as O₂⁺ and O⁺) ion escape are generally consistent with magnetohydrodynamics model predictions⁵³. Because the escape rate depends on age, we adopt a parametric model⁵⁴ that fits the ion escape rates of the MAVEN-validated magnetohydrodynamics model⁵³ to a power law of the age. The ion loss rate, F_{ion} , is thus modelled as

$$F_{\text{ion}} = \frac{X_{\text{N}_2}}{X_{\text{O},\text{N}_2} X_{\text{O},\text{CO}_2^+}} F_{0,\text{ion}} (\text{CO}_2^+) \left(\frac{t}{4,500} \right)^{-3.51}, \quad (11)$$

where X_{N_2} and $X_{\text{O},\text{CO}_2^+}$ are the present-day mixing ratios measured by MAVEN at the altitude of 160 km (ref.⁵⁵), $F_{0,\text{ion}}$ (CO₂⁺) is the present-day ion escape rate of CO₂⁺ from the parametric model⁵⁴ and the last term accounts for the evolution of the solar EUV flux with the power-law index from the parametric model⁵⁴. Similar to sputtering, the fractionation factor of ion loss is α_{diff} .

MAVEN observations indicated an approximately one-order-of-magnitude increase in the ion escape fluxes during a large interplanetary coronal mass ejection (ICME) event, while the observations took place at sparse locations⁵¹. The ensemble collections of MAVEN's ion observations during ICME events indicated that ICMEs result in a general decrease in the loss rate upstream, at low solar zenith angle (SZA), and an increase downstream, at higher SZA⁵². Integrating over SZA, these observations produced a net factor-of-two enhancement in the loss rate, although most of the events in this sample are small events. The young Sun probably produced more flare events and thus had a larger impact on the atmospheric loss. We do not include a multiplication factor in equation (11) because the total amount of N₂ lost from 3.8 Ga to the present day via ion loss is less than by sputtering by several orders of magnitude. Thus, a variation in the ion loss rate by an order of magnitude would not change our model. We instead explore the sputtering multiplier f_{sp} in a wide range that captures the uncertainty in the pickup ion flux affected by solar activities.

Nitrate formation. See Supplementary Information C.

Volcanic outgassing. We estimate the volcanic outgassing flux (F_{og}) from the history of crustal formation and the N₂ content in the source magma. We model this as

$$F_{\text{og}} = V \rho_{\text{cr}} x_{\text{N}_2} f_{\text{og}}, \quad (12)$$

where V is the crustal production rate, ρ_{cr} is the density of the crust, x_{N_2} is the concentration of N₂ in the source magma and f_{og} is a multiplication factor that accounts for the uncertainty in the crustal formation rate (including the extrusive-to-intrusive ratio) and the uncertainty in the outgassing efficiency.

For the crustal production rate, we combine the thermal evolution model estimate (the 'global melt' scenario in ref.⁵⁰) and the photogeological analysis of volcanic provinces on the planet's surface⁵⁷ (Extended Data Fig. 3). The outgassing factor in our evolution model f_{og} is directly comparable to the outgassing factor in the argon evolution model (the parameter v_f in ref.¹⁵). The crustal production rate in our model is highest at 3.8 Ga and remains quite high throughout the Hesperian period. The total volume of volcanic emplacement between 3.8 and 3.0 Ga in our baseline model is approximately $4 \times 10^8 \text{ km}^3$, compared with $3 \times 10^8 \text{ km}^3$ as the estimated volume of the Tharsis Rise⁵⁸. Our volcanic outgassing model is thus consistent—within a factor of a few and captured by the multiplication parameter f_{og} —with the recently revised picture that major volcanic emplacements such as the Tharsis Rise occurred during the late Noachian and the Hesperian^{59,60}. Our volcanic model includes a non-negligible rate in the Amazonian, particularly within the past 500 Myr. This is also consistent with the geological evidence for active volcanism until very recently (0.1 Ga (ref.⁶¹)).

Unlike carbon, whose concentration in the magma is limited by its solubility²⁶, the concentration of N₂ in the magma is typically not solubility limited and thus reflects the formation history of the planet itself. In this work we adopt the 'silicate

Earth' concentration²⁵ ($x_{\text{N}_2} = 1.9 \times 10^{-6}$) as the baseline value and recognize that Mars may have a different amount of nitrogen in the first place and may have a non-uniform distribution of nitrogen in the mantle. The uncertainty in x_{N_2} can be absorbed into the factor f_{og} .

Volcanic outgassing introduces fresh nitrogen into the atmosphere and causes its isotopic composition to change with bulk mixing. The isotopic ratio, $\delta^{15}\text{N}$, is modelled as

$$\delta^{15}\text{N} = \frac{P_{\text{og}} \delta^{15}\text{N}_{\text{mantle}} + P_{\text{atm}} \delta^{15}\text{N}}{P_{\text{og}} + P_{\text{atm}}}, \quad (13)$$

where P_{og} is the partial pressure of N₂ outgassed per time step, P_{atm} is the partial pressure of N₂ in the bulk atmosphere and $\delta^{15}\text{N}_{\text{mantle}}$ is the isotopic composition of nitrogen in the mantle. We assume $\delta^{15}\text{N}_{\text{mantle}}$ to be the value measured in the Martian meteorite ALH 84001³. Two isotopically distinct components of nitrogen have been found in ALH 84001³. The lighter one ($\delta^{15}\text{N} = -30\%$) may correspond to the nitrogen from the mantle, and the slightly evolved one ($\delta^{15}\text{N} = 7\%$) may correspond to the early Martian atmosphere.

MCMCs. We employ the MCMC method to explore the vast parameter space of the evolution model. The likelihood function (L) defined for the MCMC analysis is

$$\log L = \left(\frac{P_{0,\text{observed}} - P_{0,\text{model}}}{\sigma_p} \right)^2 + \left(\frac{\delta_{0,\text{observed}} - \delta_{0,\text{model}}}{\sigma_\delta} \right)^2, \quad (14)$$

where δ represents $\delta^{15}\text{N}$ and σ is the uncertainty for the current size and composition of the free nitrogen reservoir. Because the current size is ~0.12–0.13 mbar including the regolith adsorption, we adopt the centre value of $P_{0,\text{observed}} = 0.125$ mbar and the uncertainty of $\sigma_p = 0.0017$ mbar. Essentially, this gives the nonzero denominator required in the likelihood function, and the small value for σ_p means that any successful model must match with the present-day atmospheric pressure. For the isotopic composition, we use the values measured by Curiosity's Sample Analysis at Mars instrument⁴: $\delta_{0,\text{observed}} = 572\%$ and $\sigma_\delta = 82\%$.

The seven parameters listed in Table 1 are included as the free parameters in the MCMC simulations, and they have flat prior distributions in the ranges in which they are allowed to vary. For each MCMC simulation, two 2,000,000-element chains are produced starting from the parameters chosen independently and randomly within the allowed ranges. These two chains are then tested for convergence using the Gelman–Rubin method⁶² and, if converged, combined to derive the posterior distributions.

Data availability

The data needed to generate all figures in the main text (Figs. 1–3) and Extended Data Figs. 2 and 3 are publicly available at Zenodo (<https://doi.org/10.5281/zenodo.5760095>).

Code availability

The source code of the nitrogen evolution model and the associated configuration files used in this study are publicly available at Zenodo (<https://doi.org/10.5281/zenodo.5760095>).

References

34. Zent, A., Quinn, R. & Jakosky, B. Fractionation of nitrogen isotopes on Mars: the role of the regolith as a buffer. *Icarus* **112**, 537–540 (1994).
35. Ballou, E. V., Wood, P. C., Wydeven, T., Lehwalt, M. E. & Mack, R. E. Chemical interpretation of Viking Lander 1 life detection experiment. *Nature* **271**, 644–645 (1978).
36. Nakamura, T. & Tajika, E. Climate change of Mars-like planets due to obliquity variations: implications for Mars. *Geophys. Res. Lett.* **30**, 1685 (2003).
37. Soto, A., Mischna, M., Schneider, T., Lee, C. & Richardson, M. Martian atmospheric collapse: idealized GCM studies. *Icarus* **250**, 553–569 (2015).
38. Ribas, I., Guinan, E. F., Güdel, M. & Audard, M. Evolution of the solar activity over time and effects on planetary atmospheres. I. High-energy irradiances (1–1700 Å). *Astrophys. J.* **622**, 680 (2005).
39. Claire, M. W. et al. The evolution of solar flux from 0.1 nm to 160 μm: quantitative estimates for planetary studies. *Astrophys. J.* **757**, 95 (2012).
40. Tu, L., Johnstone, C. P., Güdel, M. & Lammer, H. The extreme ultraviolet and X-ray Sun in time: high-energy evolutionary tracks of a solar-like star. *Astron. Astrophys.* **577**, L3 (2015).
41. Bakalian, F. Production of hot nitrogen atoms in the Martian thermosphere. *Icarus* **183**, 69–78 (2006).
42. Bakalian, F. & Hartle, R. E. Monte Carlo computations of the escape of atomic nitrogen from Mars. *Icarus* **183**, 55–68 (2006).
43. Cui, J., Wu, X.-S., Gu, H., Jiang, F.-Y. & Wei, Y. Photochemical escape of atomic C and N on Mars: clues from a multi-instrument MAVEN dataset. *Astron. Astrophys.* **621**, A23 (2019).
44. Lillis, R., Frey, H. & Manga, M. Rapid decrease in Martian crustal magnetization in the Noachian era: implications for the dynamo and climate of early Mars. *Geophys. Res. Lett.* **35**, L14203 (2008).

45. Luhmann, J., Johnson, R. & Zhang, M. Evolutionary impact of sputtering of the Martian atmosphere by O⁺ pickup ions. *Geophys. Res. Lett.* **19**, 2151–2154 (1992).
46. Fang, X. et al. The importance of pickup oxygen ion precipitation to the Mars upper atmosphere under extreme solar wind conditions. *Geophys. Res. Lett.* **40**, 1922–1927 (2013).
47. Wang, Y.-C. et al. Statistical studies on Mars atmospheric sputtering by precipitating pickup O⁺: preparation for the MAVEN mission. *J. Geophys. Res. Planets* **120**, 34–50 (2015).
48. Leblanc, F. et al. Mars heavy ion precipitating flux as measured by Mars atmosphere and volatile evolution. *Geophys. Res. Lett.* **42**, 9135–9141 (2015).
49. Leblanc, F. & Johnson, R. Sputtering of the Martian atmosphere by solar wind pick-up ions. *Planet. Space Sci.* **49**, 645–656 (2001).
50. Barabash, S., Fedorov, A., Lundin, R. & Sauvaud, J.-A. Martian atmospheric erosion rates. *Science* **315**, 501–503 (2007).
51. Jakosky, B. M. et al. MAVEN observations of the response of Mars to an interplanetary coronal mass ejection. *Science* **350**, aad0210 (2015).
52. Curry, S. et al. Observations of ICMEs at Mars: past and present. *AGU Fall Meeting Abstracts* **2018**, P51H--2971 (2018).
53. Ma, Y.-J. & Nagy, A. F. Ion escape fluxes from Mars. *Geophys. Res. Lett.* **34**, L08201 (2007).
54. Manning, C. V., Ma, Y., Brain, D. A., McKay, C. P. & Zahnle, K. J. Parametric analysis of modeled ion escape from Mars. *Icarus* **212**, 131–137 (2011).
55. Bougher, S. et al. Early MAVEN deep dip campaign reveals thermosphere and ionosphere variability. *Science* **350**, aad0459 (2015).
56. Grott, M., Morschhauser, A., Breuer, D. & Hauber, E. Volcanic outgassing of CO₂ and H₂O on Mars. *Earth Planet. Sci. Lett.* **308**, 391–400 (2011).
57. Greeley, R. & Schneid, B. D. Magma generation on Mars: amounts, rates, and comparisons with Earth, Moon, and Venus. *Science* **254**, 996–998 (1991).
58. Phillips, R. J. et al. Ancient geodynamics and global-scale hydrology on Mars. *Science* **291**, 2587–2591 (2001).
59. Tanaka, K. L., Robbins, S., Fortezzo, C., Skinner, J. Jr. & Hare, T. M. The digital global geologic map of Mars: chronostratigraphic ages, topographic and crater morphologic characteristics, and updated resurfacing history. *Planet. Space Sci.* **95**, 11–24 (2014).
60. Bouley, S., Baratoux, D., Paulien, N., Missenard, Y. & Saint-Bézar, B. The revised tectonic history of Tharsis. *Earth Planet. Sci. Lett.* **488**, 126–133 (2018).
61. Werner, S. C. The global Martian volcanic evolutionary history. *Icarus* **201**, 44–68 (2009).
62. Gelman, A. et al. Inference from iterative simulation using multiple sequences. *Stat. Sci.* **7**, 457–472 (1992).
63. Laskar, J. et al. Long term evolution and chaotic diffusion of the insolation quantities of Mars. *Icarus* **170**, 343–364 (2004).
64. Manning, C. V., McKay, C. P. & Zahnle, K. J. The nitrogen cycle on Mars: impact decomposition of near-surface nitrates as a source for a nitrogen steady state. *Icarus* **197**, 60–64 (2008).
65. Werner, S. & Tanaka, K. Redefinition of the crater-density and absolute-age boundaries for the chronostratigraphic system of Mars. *Icarus* **215**, 603–607 (2011).
66. Ivanov, B. A. Mars/Moon cratering rate ratio estimates. *Space Sci. Rev.* **96**, 87–104 (2001).
67. Hartmann, W. K. Martian cratering 8: isochron refinement and the chronology of Mars. *Icarus* **174**, 294–320 (2005).

Acknowledgements

We thank Y. L. Yung, B. Ehlmann, B. Jakosky, H. Kurokawa, C. Manning, R. Johnson, M. Grott, F. Gaillard, M. Slipski and C.-Y. Ng for helpful discussions. This work was supported by NASA Habitable Worlds grant NNN13D466T, later changed to 80NM0018F0612. The research was carried out at the Jet Propulsion Laboratory, California Institute of Technology, under a contract with the National Aeronautics and Space Administration.

Author contributions

R.H. designed the study and the evolution model, interpreted the results and wrote the manuscript. T.B.T. implemented the evolution model, carried out the simulations and interpreted the results.

Competing interests

The authors declare no competing interests.

Additional information

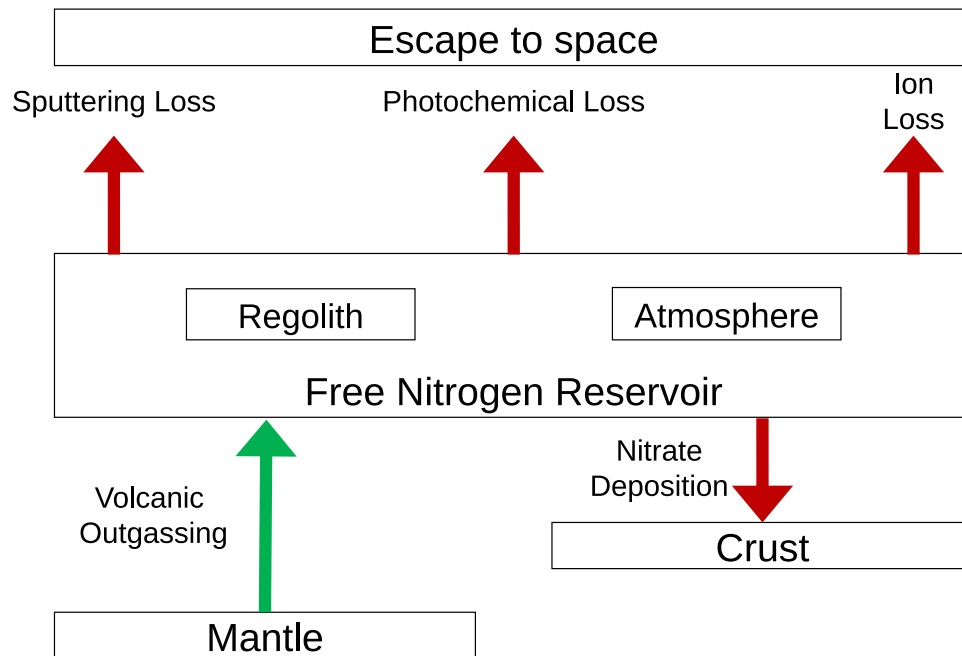
Extended data is available for this paper at <https://doi.org/10.1038/s41561-021-00886-y>.

Supplementary information The online version contains supplementary material available at <https://doi.org/10.1038/s41561-021-00886-y>.

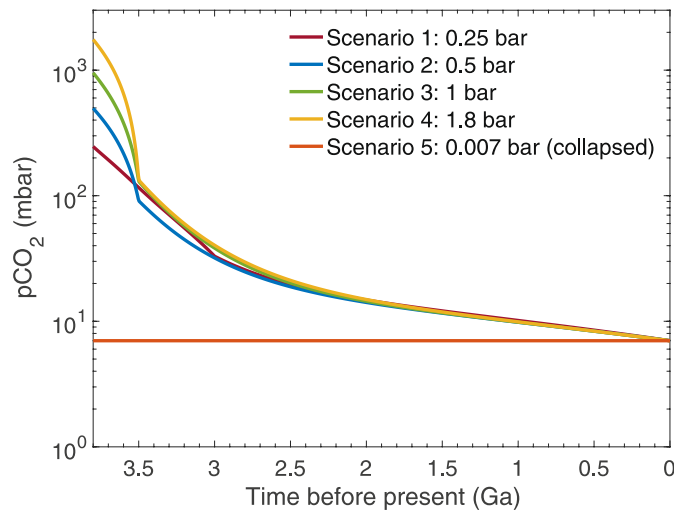
Correspondence and requests for materials should be addressed to Renyu Hu.

Peer review information *Nature Geoscience* thanks Ramses Ramirez and the other, anonymous, reviewer(s) for their contribution to the peer review of this work. Primary Handling Editors: Tamara Goldin; Xujia Jiang; Stefan Lachowycz.

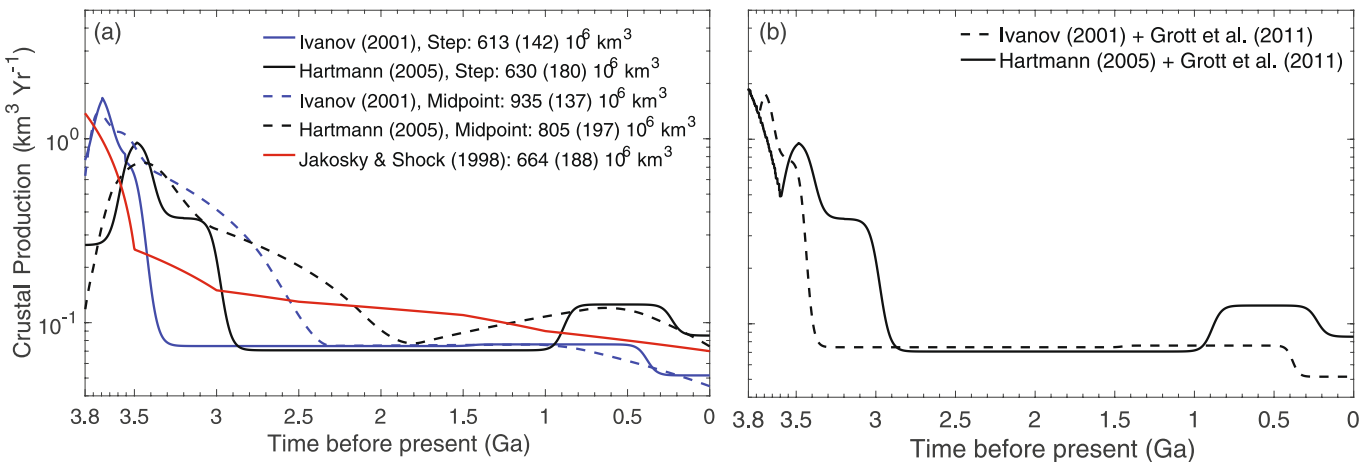
Reprints and permissions information is available at www.nature.com/reprints.



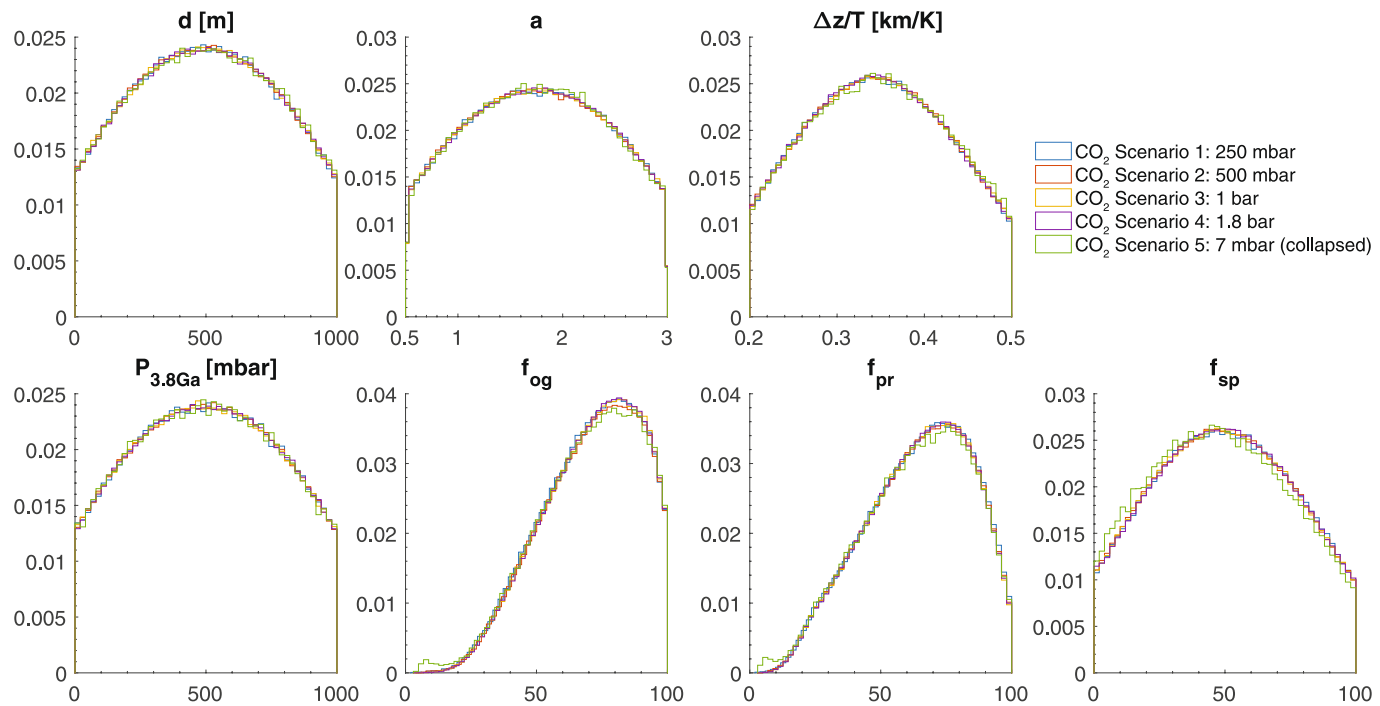
Extended Data Fig. 1 | A model for the long-term evolution of the free nitrogen reservoir on Mars. The free nitrogen reservoir is comprised of N₂ adsorbed in the regolith and ₂ in the atmosphere, and it changes over time due to sputtering loss, photochemical loss, ion loss, volcanic outgassing, and nitrate deposition. The regolith and the atmosphere are assumed to exchange isotopes over geologic timescales driven by the temperature variations due to orbital obliquity changes⁶³. We do not include impact additions or removal because the major impacts should have occurred before the modeled period^{1,2} (from 3.8 Ga to present). Nor do we include the impact decomposition of near-surface nitrates⁶⁴ explicitly, as its rate is less than the present-day outgassing and photochemical escape rates by several orders of magnitude (Supplementary Information H).



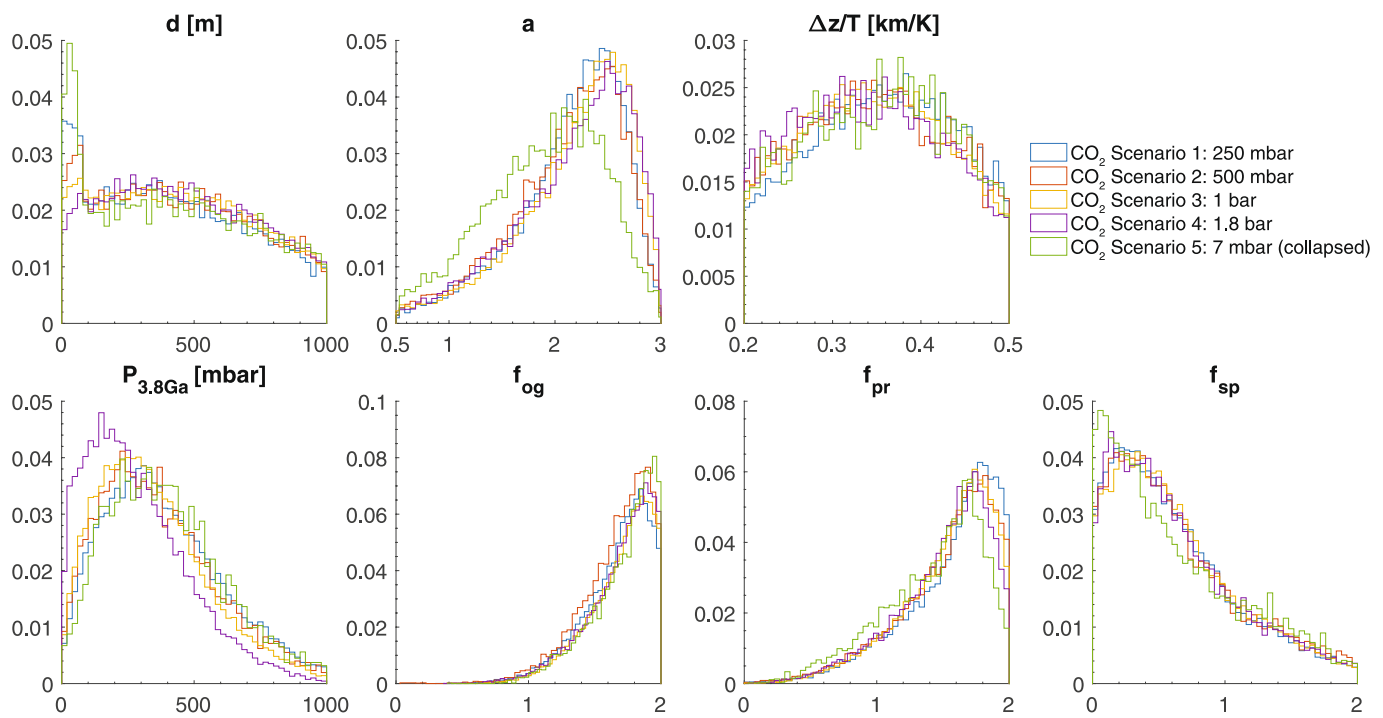
Extended Data Fig. 2 | Representative background CO_2 evolutionary scenarios adopted in this study. These scenarios are selected from the evolutionary tracks of CO_2 derived in Hu et al. (2015)¹⁶ and they are consistent with the present-day pressure and carbon isotopic composition. Scenarios 1 - 3 assume that the photochemical loss rate of carbon depends on the Sun's Lyman continuum flux to the power of 2. Scenario 1 assumes that carbonate deposition of 40 mbar occurred throughout the Noachian and Hesperian (that is, till 3.0 Ga) in shallow subsurface aquifers. This represents the lower bound of the initial CO_2 partial pressure. Scenarios 2 and 3 assume that carbonate deposition of 290 and 600 mbar occurred in the Noachian and early Hesperian (that is, till 3.5 Ga) in open-water systems. Scenario 3 has an initial CO_2 partial pressure of 1 bar and is the default scenario adopted in this study. Scenario 4 assumes a power-law index of 3, and that carbonate deposition of 1400 mbar occurred in the Noachian and early Hesperian (that is, till 3.5 Ga) in open-water systems. This represents the upper bound of the initial CO_2 partial pressure. Scenario 5 is an endmember scenario where the CO_2 atmosphere is assumed to be collapsed at all times and the pressure constant at 7 mbar.



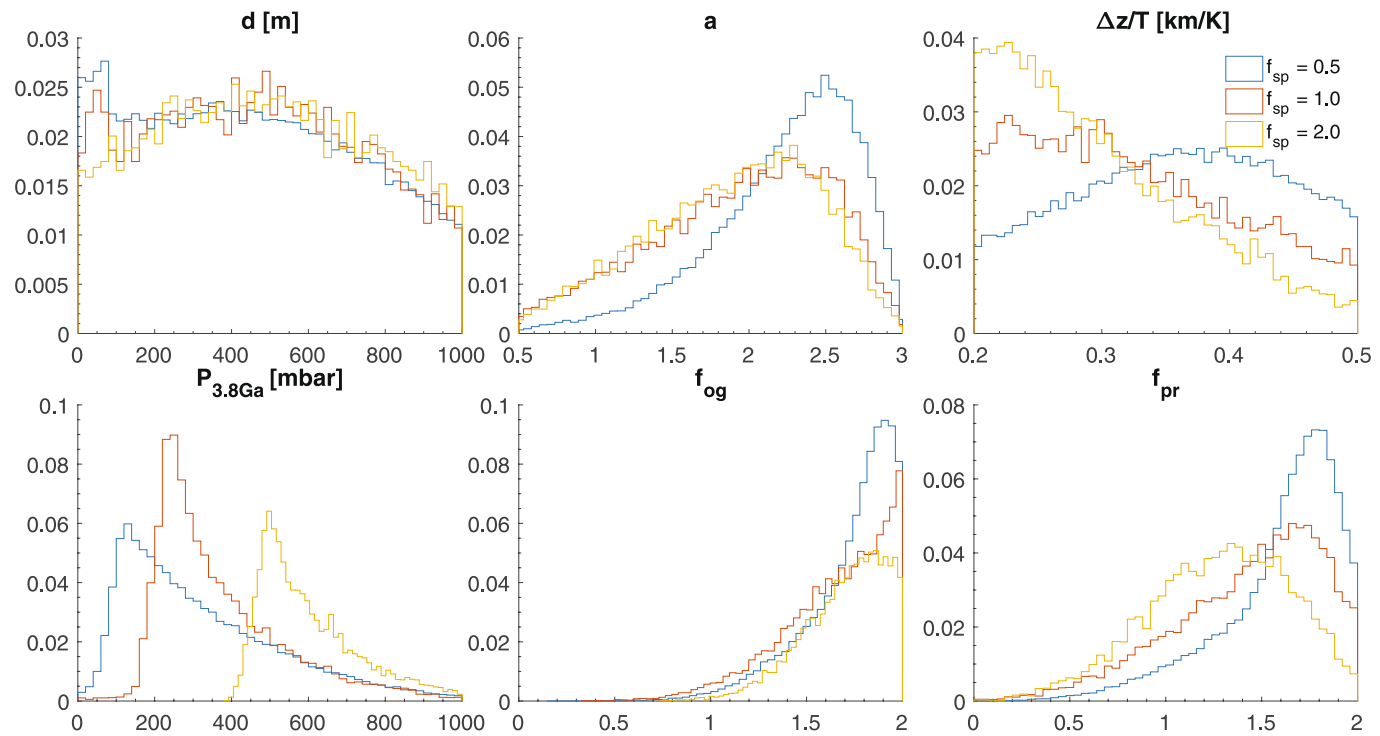
Extended Data Fig. 3 | Baseline crustal production rate adopted in this study. (a) Crustal production rates derived from the photogeologic analysis of volcanic provinces⁵⁷ from 3.8 Ga. To convert the photogeological analysis (expressed as the total volcanic emplacement in each geologic period from middle Noachian to late Amazonian) to the crustal production rate, we compare the rates derived using the age boundaries from the crater density⁶⁵ and the chronology model of Ivanov (2001)⁶⁶ and Hartmann (2005)⁶⁷, as well as interpolation methods using either step functions or mid-point averages. The labels show the total volcanic activity and the integrated volcanic activity in the last 2 billion years (in parentheses). The midpoint approach would introduce substantially more total volcanism, and so we use the step-function approach. Also in comparison is a volcanic history derived from earlier photogeologic analyses and used in the recent argon isotope study¹⁵. The step-function approach on the Hartmann (2015) chronology leads to a baseline model that is very similar to the one used in the argon isotope study¹⁵ in terms of the total and the recent volcanic rates. (b) Baseline crustal production rate adopted in this work, based on the global thermal evolution model⁵⁶ and the step-function interpolation of the photogeologic analysis of volcanic provinces⁵⁷, whichever is greater. We adopt the model using the Hartmann (2015) chronology as our baseline model, and consider the one using the Ivanov (2001) chronology as the variant. The two models have appreciable difference in the last 2 billion years.



Extended Data Fig. 4 | Posterior distributions of parameters from unconstrained MCMC simulations with the parameters and their boundaries listed in Table 1. The MCMC simulations adopt the five representative CO_2 evolution scenarios shown in Extended Data Fig. 2.



Extended Data Fig. 5 | Posterior distributions of parameters from constrained MCMC simulations with the parameters and their boundaries listed in Table 1. The MCMC simulations adopt the five representative CO_2 evolution scenarios in Extended Data Fig. 2.



Extended Data Fig. 6 | Posterior distributions of parameters from constrained MCMC simulations that fix the sputtering multiplier to be $f_{sp}=0.5, 1$, and 2 . These simulations adopt the CO₂ evolutionary scenario No. 3 with the initial partial pressure of 1.0 bar as shown in Extended Data Fig. 2. The initial partial pressure of N₂ is more tightly constrained when the sputtering multiplier is fixed.